

Exploring the complex free energy landscape of the simplest glass by rheology

Yuliang Jin¹ and Hajime Yoshino^{1,2}

¹*Cybermedia Center, Osaka University, Toyonaka, Osaka 560-0043, Japan*

²*Graduate School of Science, Osaka University, Toyonaka, Osaka 560-0043, Japan*

The essence of the traditional view on solids is that they can be described in terms of the ground state and harmonic low energy excitations on top of it, such as phonons. While this is established for crystals, the validity of the simple harmonic picture for amorphous solids has been a subject of intense debates [1–15]. Recent emerging developments of a class of first-principle theory of amorphous solids [16, 17] revealed the possibility of unexpectedly complex free energy landscape where the traditional harmonic picture is predicted to break down [10, 14]. Here we demonstrate that a standard rheological technique can be used as a powerful tool to explore the complex free energy landscape and examine the intriguing theoretical predictions. By performing extensive numerical simulations on a hard sphere glass under quasi-static shear at finite temperatures, we show that, above the so-called Gardner transition density, the elasticity breaks down, the stress relaxation exhibits slow and aging dynamics, and the apparent shear modulus becomes protocol-dependent. Being designed to be reproducible in the laboratory, our approach may open the door to explore the complex free energy landscapes of a large variety of amorphous materials.

Amorphous and crystalline solids have very different behaviors under external perturbations. It is well known that by increasing the shear strain, a crystal displays a linear elastic response, followed by plastic deformation and yielding. Experiments and numerical simulations show that this picture breaks down for amorphous solids, such as glasses [2, 5, 6, 15, 18], granular matter [3, 11, 13], and foams [4], where the elastic behavior is mixed with plastic events. Such plastic events cause sudden drops in stress-strain curves, and are sometimes referred to as crackling noise [19], due to their similarities to avalanches in earthquakes. An apparent shear modulus or *rigidity* μ , which is the ratio between the stress and strain, can be nevertheless defined and measured. Experiments on glassy emulsion systems [20, 21] show that μ scales linearly $\mu \sim P$ with the pressure P both below and above the jamming density, while harmonic treatments predict $\mu \sim P^{1.5}$ (below) [22] and $\mu \sim P^{0.5}$ (above) [23] respectively. These contradictions reveal that amorphous solids can be strikingly softer than purely harmonic solids like crystals, even at sufficiently low temperatures where the harmonic expansion was conventionally expected to be valid.

On the theoretical side, the mean-field theory based on the exact solution in the large dimensional limit of the hard sphere glass has brought a more accurate and comprehensive picture beyond the harmonic description [16]. The main outcome is the prediction of a Gardner transition (see Fig. 1a), which divides the classical amorphous phase into two: in the *stable phase* (or *normal phase*), the state is confined in one of the simple smooth basins on the free energy landscape; once the system is compressed above the Gardner transition density φ_G (or is cooled down below the Gardner transition temperature T_G), the simple glass basin splits into a fractal hierarchy of sub-basins and the glass state becomes marginally stable. Interestingly, recent theories point out that the elastic anomalies should only appear in the *marginal stable phase* (or *Gardner phase*) [10, 14]. Here we test this appealing proposal, and compare quantitatively the scaling laws predicted by the theory with numerical data. We design laboratory reproducible protocols, and apply them on densely packed hard spheres, which is a simple and representative glass-forming model. In the present letter, however, we do not attempt to judge whether the Gardner transition survives in finite dimensional systems as a sharp phase transition or becomes a crossover (in the thermodynamic limit), but rather we aim to explore the possibilities to observe its non-trivial signatures in experimentally feasible length/time scales. To avoid crystallization, we work on a polydisperse mixture of hard spheres whose diameters are distributed according to a probability distribution $P(D) \sim D^{-3}$, for $D_{\min} \leq D < D_{\min}/0.45$ [24, 25]. The Gardner transition of this model has been detected by characterizing the growing time and length scales associated to the thermal vibrations of particles [25].

Breakdown of elasticity – We design a numerical protocol to mimic a simple shear experiment of deeply annealed glasses (see Fig. 1). A glass is typically obtained by a slow compression (or cooling) annealing from a dilute state, where it falls out of equilibrium at the compression (or cooling) rate-dependent glass transition density φ_g (or glass transition temperature T_g). Since we choose hard spheres as our working system, the density is the control parameter. Our protocol includes three steps: (i) We first use the swap algorithm [24, 25] to prepare a well-equilibrated supercooled-liquid configuration at various densities φ_g (see Appendix). The algorithm combines the Lubachevsky-Stillinger algorithm [26], which consists of standard event-driven molecular dynamics (MD) and slow compression, with Monte-Carlo swaps of particle diameters. At a given density φ_g , we prepare many of such equilibrated configurations, which are statistically independent from each other, and we call them *samples* in the following. From the thermodynamic

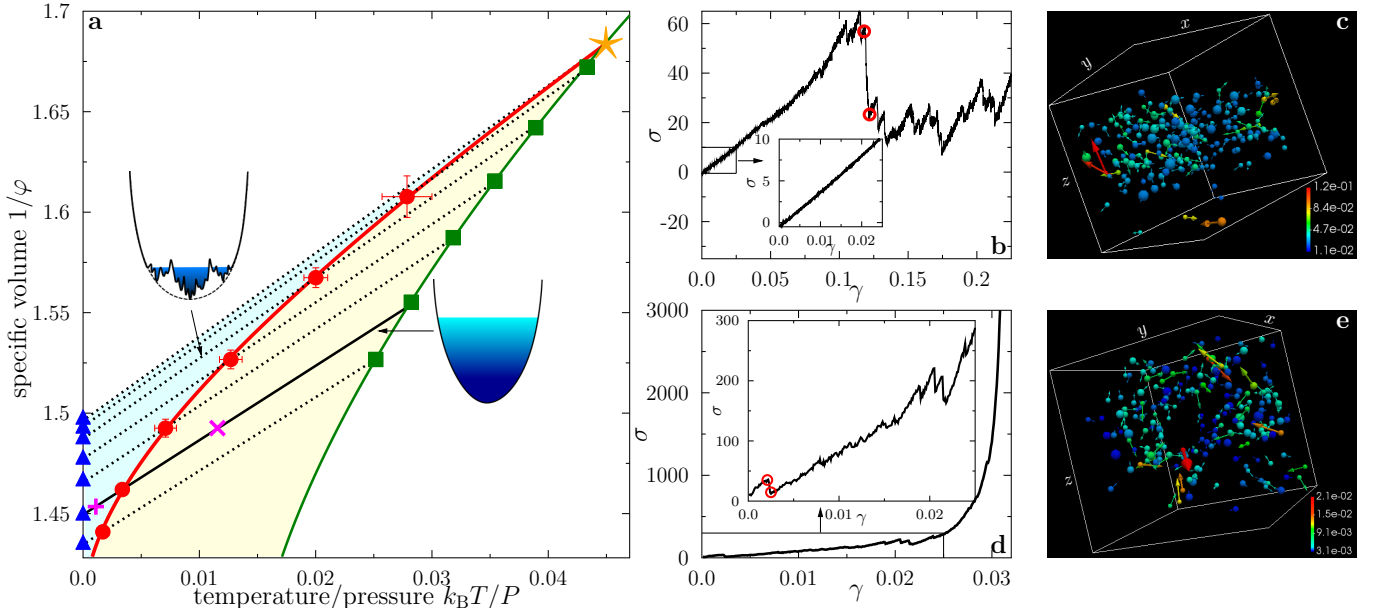


FIG. 1. **Typical stress responses under quasi-static shear.** (a) Illustration of the protocol on the polydisperse hard sphere glass phase diagram (adapted from Ref. [25]), where $k_B T/P = 1/(\rho p)$. The MCT dynamical crossover (yellow star) is located at $\phi_d = 0.594(1)$ along the equilibrium liquid equation of state (EOS, green line). Using the swap algorithm we first prepare equilibrium samples at various densities ϕ_g (green squares) whose pressure obeys the liquid EOS. Next we switch off the swap algorithm, and perform compression annealing from ϕ_g to jamming (blue triangles), producing realizations of compressed glasses at various densities ϕ . The system is now out-of-equilibrium and the pressure follows the glass EOSs (black dotted lines). The Gardner transition ϕ_G (red circles and line) separates the stable (light yellow regime) and the marginally stable (light blue regime) glass phases. The insets show schematic depictions of free energy landscapes in these two different phases. As an example, an equilibrium configuration is prepared at $\phi_g = 0.643$, and compressed (solid black line) up to $\phi_J = 0.690(1)$. We show typical stress-strain curves under quasi-static shear, using single realizations of the compressed glass of $N = 1000$ particles, at (b) $\phi = 0.670$ (pink cross) and (d) $\phi = 0.688$ (pink plus), which are below and above $\phi_G = 0.684(1)$ respectively. Curves in (b) and (d) are zoomed in (insets) for $\gamma \leq 0.025$, to show the different small- γ behaviors in the two cases. The real-space vector fields of particle displacements are visualized in (c) for a yielding event (red circles in (b)), and (e) for a micro-yielding event (red circles in (d)), where each sphere locates at the equilibrium position before yielding/micro-yielding, and each vector represents the displacement during yielding/micro-yielding. We have subtracted the affine part caused by shear from the displacements, and only show top 20% particles with large displacements. A shear band around the middle of the z -axis is observed in (c). The sizes of particles are reduced by a factor of 0.4, and the vectors are amplified in length by a factor of 2 in (c) and a factor of 15 in (e). The color represents the magnitude of displacement.

point of view, the system is still in the liquid but we work at density ϕ_g sufficiently above the mode-coupling theory (MCT) crossover density ϕ_d . Then once we switch off the particle swapping and return to the natural dynamics simulated by MD, the α -relaxation time becomes much larger than our simulation time scales so that the system behaves essentially as a solid. This glass is thus ultrastable, in a sense similar to those obtained by vapour deposition experiments [27–29]. (ii) Subsequently the equilibrated configuration is compressed up to a target density ϕ with a compression rate $\delta_g = 10^{-3}$. From a single sample, that is a starting equilibrated configuration at ϕ_g , we generate an ensemble of compressed glasses at ϕ , obtained by choosing statistically independent initial particle velocities drawn from the Maxwell-Boltzmann distribution. We call each of such compressed glasses as a *realization* in the following. (iii) For a given realization, a simple shear is applied. The simple shear is modelled by an affine deformation of the x -coordinates of all particles, $x_i \rightarrow x_i + \gamma z_i$, under the Lees-Edwards boundary condition with fixed system volume. The shear strain is increased quasi-statically with a constant shear rate $\dot{\gamma} = 10^{-4}$ (see Appendix for a discussion on the $\dot{\gamma}$ -dependence), and the shear stress Σ is measured at different γ . The shear stress Σ and the pressure P are both calculated from inter-particle interactions due to collisions between hard sphere particles (see Appendix). For convenience, we introduce reduced pressure $p = \beta P/\rho$ and reduced stress $\sigma = \beta \Sigma/\rho$, where $\beta = 1/(k_B T)$ (set to unity) is the inverse temperature and ρ is the number density of the particles (see Appendix). Note that as the pressure, the shear stress is entirely due to momentum exchanges between the particles so that the rigidity is purely entropic in hard sphere systems.

Figure 1 shows the phase diagram for our polydisperse hard sphere model, and typical stress-strain curves of

individual realizations in different density regimes. (i) In the stable glass phase $\varphi_g < \varphi < \varphi_G$ (Fig. 1b), the stress-strain curve shows a smooth linear (harmonic) response regime at small γ , followed by a sharp drop of the stress σ , signalling the yielding of the system. At yielding, a system-wide shear band emerges (see Fig. 1c), and the system is driven out of a free energy metastable glass basin. After yielding, it becomes a fluid, such that different basins are explored freely. (ii) In the Gardner phase $\varphi_G < \varphi < \varphi_J$ the harmonic response is punctuated by *micro-yieldings* that can happen at very small γ (see Fig. 1d). These micro-yieldings correspond to sudden avalanche-like heterogeneous rearrangements of particle positions without formation of band-like patterns (see Fig. 1e). Note that similar micro-yieldings have been observed in quasi-static shear simulations at zero temperatures [2, 6], but our simulations are performed at finite temperatures.

For large φ , the stress σ grows dramatically at large γ , and appears to diverge (see Fig. 1d). This *shear jamming* phenomenon is due to the dilatancy effect of hard sphere glasses under shear: the pressure p increases with γ when the system volume is fixed. Note that if p is kept as a constant when γ is increased, then the volume expands due to the dilatancy effect. In that case, shear jamming does not appear and shear yielding is recovered (see Appendix). While the switching from shear yielding to shear jamming with increasing φ is not a consequence of the Gardner transition, it implies that the system is trapped more deeply in the metastable basin, and that the activated barrier-crossing between metastable basins becomes forbidden. However, the emergence of sub-basins in the Gardner phase implies that even though the usual relaxation (α -relaxation) is frozen, an additional slow dynamics may appear. This aspect is explored below.

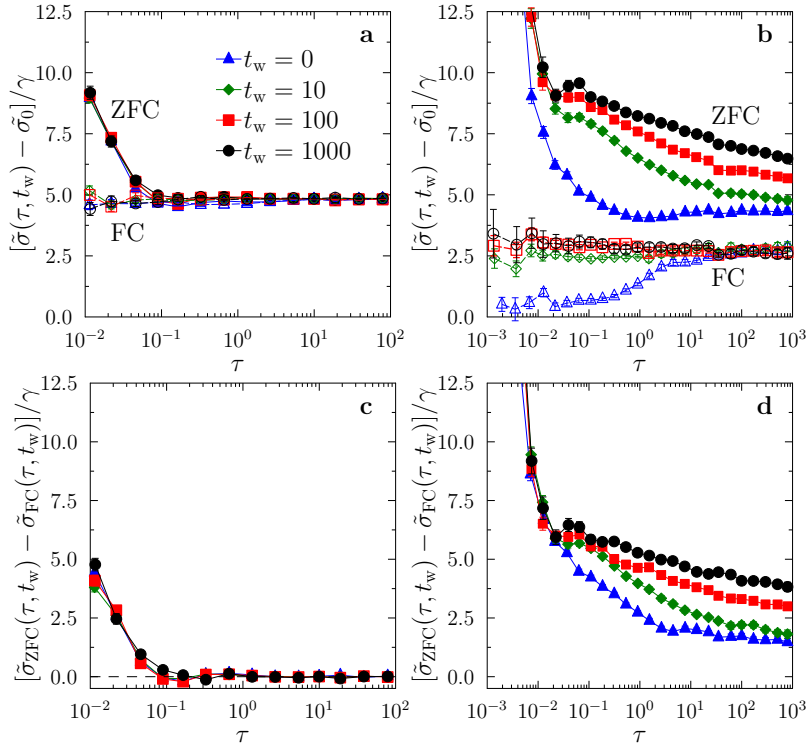


FIG. 2. **Relaxation of shear stress.** Relaxations of the rescaled ZFC shear stress $\tilde{\sigma}_{ZFC} = \sigma_{ZFC}/p$ (filled symbols) and the rescaled FC shear stress $\tilde{\sigma}_{FC} = \sigma_{FC}/p$ (open symbols) show different behaviors at (a) $\varphi = 0.670$ and (b) $\varphi = 0.688$, corresponding to the pink plus and cross in Fig. 1 respectively. We show results for several different waiting time t_w , under an instantaneous increment of shear strain $\gamma = 10^{-3}$. Data are averaged over many realizations of compressed glasses obtained from a single equilibrated sample at $\varphi_g = 0.643$ with $N = 1000$ particles. Here the rescaled remanent stress $\tilde{\sigma}_0$ is measured in the ZFC protocol at φ , after the longest waiting time $t_w = 1000$ and before the shear strain is applied. The difference $\tilde{\sigma}_{ZFC}(\tau, t_w) - \tilde{\sigma}_{FC}(\tau, t_w)$ quickly vanishes and does not show significant t_w -dependence at (c) $\varphi = 0.670$, while it decays much slower and shows a strong t_w -dependent aging effect at (d) $\varphi = 0.688$. Note that by definition, $\tilde{\sigma}_{FC}(t)$ is a one variable function, but we plot it here as $\tilde{\sigma}_{FC}(\tau, t_w)$ in order to compare it with $\tilde{\sigma}_{ZFC}(\tau, t_w)$.

Aging and slow dynamics – We next show that in the Gardner phase, the relaxation of shear stress becomes complicated, accompanied by aging and a slow dynamics. Inspired by the zero-field cooling/field cooling experiments in spin glasses [30], we use two distinct protocols which are combinations of compression and shear exerted in different orders (see Fig. 4) : In the *zero-field compression* (ZFC) protocol, we first compress the configuration from φ_g to φ ,

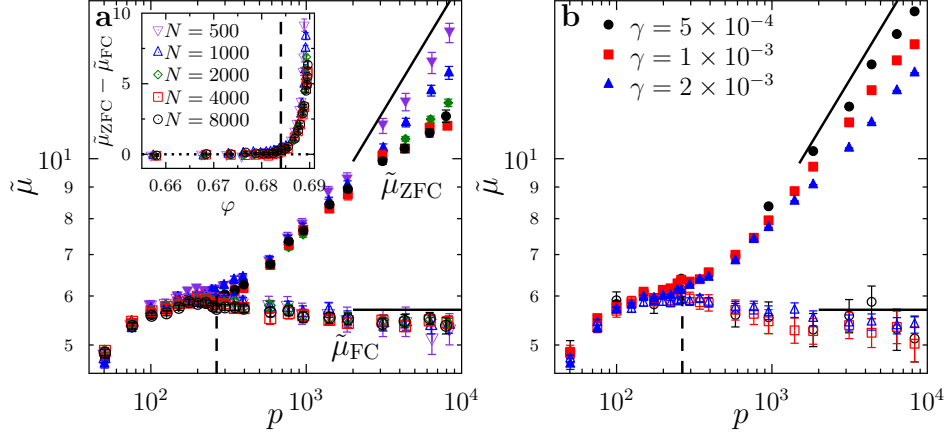


FIG. 3. **Protocol-dependent shear modulus.** (a) The rescaled shear modulus $\tilde{\mu} = \mu/p$, obtained from both ZFC (filled symbols) and FC (open symbols), is plotted as a function of p , for $\varphi_g = 0.643$ and several N . The data are obtained by using $\gamma = 2 \times 10^{-3}$, and are averaged over $N_s \approx 200$ samples, and $N_r \approx 100$ individual realizations for each sample. The two shear moduli μ_{ZFC} and μ_{FC} coincide below p_G (vertical dashed line), and become distinct above, where we use the p_G value reported in Ref. [25]. The data are compared to the large p scalings predicted by the mean-field theory $\mu_{ZFC} \sim p^{1.41574}$ and $\mu_{FC} \sim p$ (black solid lines). The difference $\mu_{ZFC} - \mu_{FC}$ is plotted as a function of φ in the inset. (b) Rescaled ZFC and FC shear moduli obtained from a few different γ , for $N = 1000$ systems.

and set the time to zero. We then wait for time t_w before a shear strain γ is applied instantaneously (see Appendix), and measure the relaxation of the stress $\sigma_{ZFC}(t, t_w)$ as a function of the time $\tau = t - t_w$ elapsed after switching on the strain. On the other hand, in the *field compression* (FC) protocol, we first apply an instantaneous increment of shear strain at the initial density φ_g , compress the configuration to φ , and set the time to zero. Then we measure the relaxation of the stress $\sigma_{FC}(t)$ as the function of the elapsed time t .

For $\varphi < \varphi_G$, $\sigma_{ZFC}(t, t_w)$ is stationary or time translationally invariant (TTI), i. e. $\sigma_{ZFC}(\tau, t_w) = \sigma_{ZFC}(\tau)$, depending only on the time difference $\tau = t - t_w$ but not on the waiting time t_w (see Fig. 2). After a time scale $\tau_{\text{cage}} \sim O(1)$ corresponding to the ballistic motions of particles [25], the ZFC stress $\sigma_{ZFC}(\tau, t_w)$ converges quickly to $\sigma_{FC}(t)$ which is almost a constant in time.

In contrast, for $\varphi > \varphi_G$, $\sigma_{ZFC}(\tau, t_w)$ displays strong t_w -dependent aging effects manifesting the out-of-equilibrium nature of the system. In such a situation, different large time limits can emerge depending on the order of $\tau \rightarrow \infty$ and $t_w \rightarrow \infty$ [31]. An important feature which can be seen in Fig. 2 is that $\sigma_{ZFC}(\tau, t_w)$ exhibits a plateau suggesting the existence of a large time limit $\sigma_{ZFC} \equiv \lim_{\tau \rightarrow \infty} \lim_{t_w \rightarrow \infty} \sigma_{ZFC}(\tau, t_w)$ where $t_w \rightarrow \infty$ is taken *before* $\tau \rightarrow \infty$. On the other hand $\sigma_{FC}(t)$ is again essentially constant in time t (for $t > \tau_{\text{cage}}$) and we shall denote it as σ_{FC} . In the reversed order of the large time limits, we expect that the ZFC shear stress decays to the FC one, $\lim_{t_w \rightarrow \infty} \lim_{\tau \rightarrow \infty} \sigma_{ZFC}(\tau, t_w) = \sigma_{FC}$. However, the convergence becomes slower as t_w increases, and its corresponding time scale could be beyond the simulation time window, as shown in the case of Fig. 2.

Apparently σ_{ZFC} is larger than σ_{FC} when $\varphi > \varphi_G$, which implies the ergodicity breaking. The aging effect and the slowing down of dynamics show the similarities between the Gardner transition and the liquid-glass transition, which demonstrates that the Gardner transition could be considered as a “glass transition” within the glass phase. In a sharp contrast, because the Gardner transition is absent in a crystal, its shear stress relaxes faster when φ increases.

Protocol-dependent shear modulus – The above observation suggests that the linear shear moduli measured by the two protocols should be distinct in the Gardner phase. We determine the shear modulus μ from the linear relations $\mu_{ZFC} = (\sigma_{ZFC} - \sigma_0)/\gamma$ and $\mu_{FC} = (\sigma_{FC} - \sigma_0)/\gamma$, where σ_0 is the remanent shear stress at φ before γ is applied. The shear strain is increased quasi-statically with rate $\dot{\gamma} = 10^{-4}$ up to a predetermined small γ . The shear stress is measured at $\tau = 1$ after waiting for $t_w = 10$. Details on the time-dependence of the shear modulus is discussed in Appendix.

Figure 3 shows that, while μ_{ZFC} and μ_{FC} are indistinguishable in the stable glass phase $\varphi < \varphi_G$ (or $p < p_G$), they become clearly distinct in the Gardner phase $\varphi > \varphi_G$ (or $p > p_G$). The bifurcation point determines the Gardner transition threshold φ_G (or p_G). Within the numerical accuracy, the φ_G determined from this approach is fully consistent with the previous estimate based on particles’ vibrational motions and caging order parameters [25]. To further test this result, we perform detailed analysis on its dependence on the number of particles N and the shear strain γ , as discussed below.

We find no appreciable finite size effects for μ_{FC} (see Fig. 3a), which is in contrast to the observation in non-

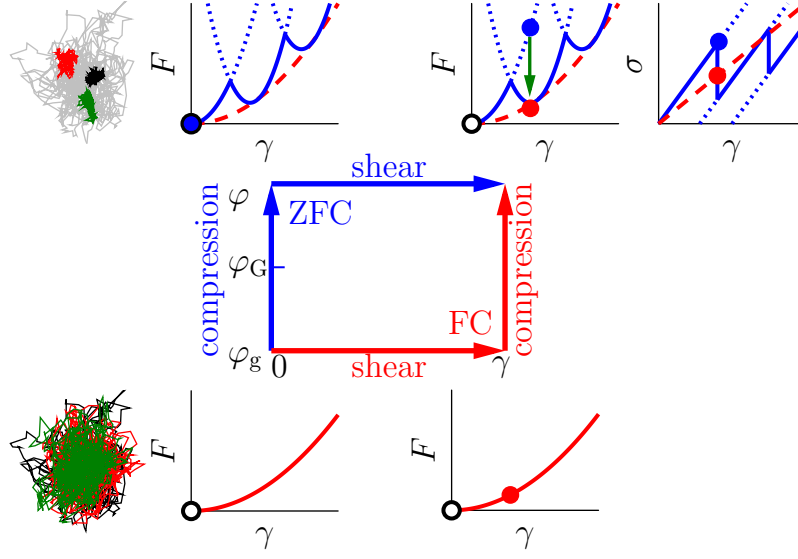


FIG. 4. **Illustration of the evolution of the free energy landscape and the state point under compression and shear.** In the ZFC protocol, the system is first compressed and then sheared, while the order is reversed in the FC protocol. (bottom-left) The schematic free energy F as a function of the strain γ at the initial density $\varphi = \varphi_g$ before compression. We assume that the initial state point (black open circle) is located at the minimum of the parabola. To show an example of the real-space particle caging, we also plot three independent trajectories of the same tagged particle in the same two-dimensional sample (see Appendix). (top-left) If the system is compressed first to φ (above the Gardner transition density φ_G), the free energy basin (red dashed line) splits into many sub-basins (blue line): the state point (blue solid circle) becomes trapped in one of the sub-basins. The dotted blue lines represent the metastable region of the sub-basins. The split of free energy basin corresponds to the split of cage in the real space. (bottom-right) On the other hand, if the system is sheared first, the state point (red solid circle) is forced to climb up the parabola of the basin. (top-right) After both shear and compression, the state point can be located at different points in the same free energy landscape, depending on the order of the compression and shear. In the ZFC case, the state point (blue solid circle) is forced to climb up the sub-basin where it is trapped, while it can remain at lower energy state in the FC protocol (red solid circle). Because sub-basins are meta-stable (dotted blue line), micro-yielding occurs with increasing γ in a quasi-static shear, and slow relaxation occurs for a fixed γ (green arrow). The shear stress σ is determined by $\sigma \sim dF/d\gamma$, and the shear modulus by $\mu = d\sigma/d\gamma \sim d^2F/d\gamma^2$. The stress-strain curves show that for $\varphi > \varphi_G$, μ_{ZFC} (slope of blue line) is larger than μ_{FC} (slope of dashed red line).

equilibrated systems, where μ_{FC} decreases to zero in the thermodynamic limit [15]. It suggests that preparing deeply equilibrium configurations is the key to observe proper finite size scalings. While the shear moduli measured around the Gardner transition, and therefore the determination of φ_G , are N -independent, stronger finite size effects are observed for μ_{ZFC} at large p near the jamming limit. Nevertheless, the data of $\mu_{ZFC}(p)$ appear to converge for $N \gtrsim 2000$, which confirms that $\mu_{ZFC}(p)$ and $\mu_{FC}(p)$ remain distinguishable in the thermodynamic limit, for $\varphi > \varphi_G$. Regarding the γ -dependence, Fig. 3b shows that, within the numerical accuracy, μ_{FC} is independent of γ , as long as γ is sufficiently small. On the other hand, for $\varphi > \varphi_G$, μ_{ZFC} slightly increases with decreasing γ . This result shows that in the Gardner phase, the non-linear effect on μ_{ZFC} remains even for very small γ , which is consistent with the observation of elasticity breakdown in Fig. 1.

For $\varphi > \varphi_g$, the mean-field theory predicts two power-law scalings in the large p limit [10]: $\mu_{ZFC} \sim p^{1.41574}$ and $\mu_{FC} \sim p$. We find good agreement between the theory and simulation on the scaling of μ_{FC} (see Fig. 3). For μ_{ZFC} , a noticeable discrepancy is observed in the limit of large N for a fixed finite γ (Fig. 3a), but the discrepancy decreases when $\gamma \rightarrow 0$ for a fixed N (Fig. 3b). The scaling $\mu_{FC} \sim p$ is consistent with the experimental observation in emulsions [20, 21]. Considering the experimental system is possibly not deeply equilibrated, we expect that the relaxation of experimental $\mu(t)$ is sufficiently fast, and the measurement was performed in the long time limit $\mu(t \rightarrow \infty) \rightarrow \mu_{FC}$ (see the discussion of Fig. 2).

Interpretation of results – The Gardner transition is a consequence of the split of glass basins in the phase space [16], and the split of particle cages in the real space (see Fig. 4). The schematic plot of the free energy F as a function of γ in Fig. 4 illustrates how a glass basin splits into many sub-basins once the system is compressed above φ_G . Here we interpret our results based on this free energy landscape viewpoint. First, in the ZFC protocol, the system intends to remain in one of the sub-basins after compression, but as γ increases in a quasi-static shear procedure (Fig. 1), it may become unstable where the shear stress drops abruptly, resulting in a micro-yielding event.

The micro-yielding could be interpreted as shear-induced barrier crossing between sub-basins, analogous to the barrier crossing between basins in a yielding event. Second, if γ is fixed, the shear stress relaxes with time, and according to the Arrhenius law, the emergence of barriers between sub-basins would result in a slowing down of the relaxation dynamics with φ (Fig. 2). The appearance of aging further reveals the emergence of complex structures within a basin, similar to the mechanism of aging in the glass transition [31]. Third, because in the FC protocol, the system can overcome the sub-basin barriers, the μ_{FC} always corresponds to the second order curvature of basins, rather than that of sub-basins as in the μ_{ZFC} case. This results in $\mu_{\text{FC}} < \mu_{\text{ZFC}}$ for the regime $\varphi > \varphi_{\text{G}}$ as observed in Fig. 3. On the other hand, no basin split occurs and therefore two protocols are equivalent in the stable phase $\varphi < \varphi_{\text{G}}$. Previous study [15] has shown that $\mu_{\text{ZFC}} = \mu_{\text{FC}}$ for crystals. The similarity between crystals and stable glasses further confirms that their free energy basins are similarly structureless.

Note that our data cannot exclude that the Gardner transition becomes just a crossover in finite dimensions, such that no real phase transition exists. Yet, irrespective of the sharpness of the Gardner transition, we rationalize here in a unified framework all the observations obtained on the rheological behavior of the simple hard sphere glass, and find quantitatively reasonable agreement between the theory and simulations. Thus, even if the Gardner transition is not sharp in the thermodynamic limit, for accessible sizes in numerical simulations, and likely for those in experiments as well [32], a behavior reminiscent of the transition can be clearly observed.

Finally, we make remarks on experimental consequences. It is an intriguing question to clarify whether the phase diagram presented in Fig. 1a is generic in a wide range of amorphous solids, ranging from different kinds of glasses to soft matter such as colloids (One can choose to change the temperature or pressure as the control parameter depending on specific systems). By analyzing particles' vibrational dynamics, a recent experiment has shown evidences of the Gardner transition in an agitated granular system [32]. However, generalizing the method to other systems, such as molecular glasses, may not be easy due to the difficulty to track the trajectories of individual particles. Our proposed ZFC/FC approach (Fig. 4) overcomes this problem, since it requires no microscopic information, but only the standard macroscopic rheological measurements that are well accessible in many experimental systems.

The crucial point is to keep track of the dynamical effects which might have been overlooked in some previous experiments, for the following two reasons. First, in reasonably stabilized dense systems, the liquid EOS (green line in Fig. 1a) and the Gardner line (red line) becomes separated enough, so that the liquid dynamics (α -relaxation) and the intriguing internal glassy dynamics (β -relaxation induced by the Gardner transition) can be well separated in time scales. In this respect, recently developed experimental techniques, such as the vapor deposition [27–29, 33] and the high pressure path [34], or the use of sufficiently old natural glasses [35], would provide ideal settings. If such an ideal setting is not possible, one could freeze the α -relaxation out of the experimental time window, by working at sufficiently low temperatures or high densities. The second reason is that by experimentally studying the aging effects due to the internal dynamics of the amorphous solids, the complexity of the free energy landscape could become manifested as we demonstrated in the present letter.

ACKNOWLEDGMENTS

We especially thank Francesco Zamponi and Daijyu Nakayama, Satoshi Okamura for many useful discussions. We also thank Giulio Biroli, Ludovic Berthier, Patrick Charbonneau, Olivier Dauchot, Anaël Lemaître, Corrado Rainone, Pierfrancesco Urbani for discussions. This work was supported by KAKENHI (No. 25103005 “Fluctuation & Structure”) from MEXT, Japan. The Computations were performed using Research Center for Computational Science, Okazaki, Japan.

Appendix A: Model and observables

We study an assembly of N polydisperse hard spheres (HSs) whose diameters are distributed according to a probability distribution [24, 25],

$$P(D) \sim D^{-3}, \quad D_{\min} \leq D < D_{\min}/0.45. \quad (\text{A1})$$

The control parameter is the number density $\rho = N/V$ or the volume fraction $\varphi = (\pi/6)\rho \int_{D_{\min}}^{D_{\min}/0.45} dD P(D) D^3$, where V is the volume of the system. The mode-coupling theory (MCT) dynamical crossover density is $\varphi_{\text{d}} = 0.594(1)$ [25]. The simulation time t is expressed in units of $\sqrt{\beta m \bar{D}^2}$, where the inverse temperature β , the particle mass m , and the mean particle diameter $\bar{D} = \int_{D_{\min}}^{D_{\min}/0.45} dD P(D) D$ all set to unity.

For a HS system, the stress is entropic. The stress tensor is given by

$$\Sigma_{mn} = -\frac{1}{V} \sum_{i < j} \mathbf{r}_{ij,m} \mathbf{f}_{ij,n} \quad (\text{A2})$$

where $\mathbf{r}_{ij,m}$ is the m -th component of the separation vector $\mathbf{r}_{ij} = \mathbf{r}_i - \mathbf{r}_j$ between particles i and j , and $\mathbf{f}_{ij,n}$ is the n -th component of the inter-particle force \mathbf{f}_{ij} . The force \mathbf{f}_{ij} is computed from the exchange rate of the momentum between i and j . In our shear protocols, we are interested in the z - x element of the stress tensor (we omit the subscript),

$$\Sigma = -\frac{1}{V} \sum_{i < j} z_{ij} \mathbf{f}_{ij,x}. \quad (\text{A3})$$

The pressure P is the negative average of three diagonal elements of the stress tensor, i.e., $P = -(\Sigma_{xx} + \Sigma_{yy} + \Sigma_{zz})/3 = \frac{1}{3V} \sum_{i < j} \mathbf{r}_{ij} \cdot \mathbf{f}_{ij}$. In this study, we report results in the units of reduced pressure $p = \beta P/\rho$ and reduced stress $\sigma = \beta \Sigma/\rho$.

Appendix B: Numerical protocols

1. Swap algorithm

To prepare dense equilibrium configurations at φ_g , we combine the Lubachevsky-Stillinger (LS) algorithm with the swap Monte Carlo moves [24, 25]. The LS algorithm uses event driven molecular dynamics with varying particle diameters. Our protocol consists of the following two steps:

1. Starting from an ideal gas configuration, we first compress it to $\varphi_0 = 0.54$, by growing spheres at a constant rate $\delta_g = 10^{-3}$, such that $D(t) = D(0)(1 + \delta_g t)$. Because the process is equivalent to compression, hereafter we call δ_g as compression rate. This initial compression is fast enough to suppress crystallization, and slow enough to equilibrate the configuration up to φ_0 .

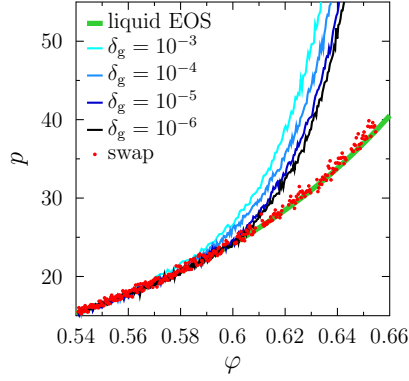


FIG. 5. Evolution of the reduced pressure p under compression, for a system of $N = 2000$ particles. The data obtained from the swap algorithm agree with the equilibrium liquid EOS. For comparison, we also plot data obtained from pure compression done by the LS algorithm without the swap for a few different compression rate δ_g . The swap algorithm falls out of equilibrium at much higher φ , compared to the standard compressions.

2. Starting from the equilibrium configuration at φ_0 , we switch to a slower compression rate $\delta_g = 10^{-5}$, and compress the configuration to a higher density φ_g . Swap attempts are introduced: we randomly pick a pair of particles and exchange their diameters if no overlap is created after the swap. The particle sizes do not change during swap moves. We perform 10% swap moves and 90% LS molecular dynamics steps. After the compression, we further relax the configuration for $t = 1000$ to check that the pressure does not change. The equation of state (EOS) of our equilibrium configurations agrees with the Carnahan-Stirling (CS) expression (see Fig. 5) [36],

$$p_{\text{CS}}(\varphi) = \frac{1}{1-\varphi} + \frac{3s_1s_2}{s_3} \frac{\varphi}{(1-\varphi)^2} + \frac{s_2^3}{s_3^2} \frac{(3-\varphi)\varphi^2}{(1-\varphi)^3}, \quad (\text{B1})$$

where s_k is the k -th moments of the diameter distribution function $P(D)$ given by Eq. (A1).

The swap algorithm is switched off once the equilibrated configuration at the target φ_g is obtained. All the subsequent simulations are performed using the molecular dynamics without the use of the swap.

2. Shear protocols

a. Quasi-static shear

In the quasi-static shear, the shear strain γ is increased with time at a constant rate $\dot{\gamma}$, which is set small enough such that the system is quasi-equilibrated at each step. The protocol consists of the following steps:

1. Increase the shear strain γ instantaneously by an infinitesimal amount $\gamma \rightarrow \gamma + \delta\gamma$ with $\delta\gamma = 10^{-4}$. We perform an affine deformation to all particles, whose positions are shifted by $x_i \rightarrow x_i + \delta\gamma z_i$, where x_i and z_i are the x - and z -coordinates of particles i . This instantaneous shift could introduce overlaps between some particles, which are removed by using the conjugated gradient (CG) method [37]. To use CG, a harmonic inter-particle potential $\varphi_{ij}(r) = (1 - r/D_{ij})^2$ (zero when $r > D_{ij}$) is used, where $D_{ij} = (D_i + D_j)/2$ is the average diameter of particles i and j . The boundary condition in the z direction satisfies the Lees-Edwards scheme [38], i.e., the x -position of the top (bottom) imaginary box is shifted by $\delta\gamma L$ ($-\delta\gamma L$), where L is the linear size of the simulation box. After this step, we obtain a non-overlapping HS configuration under shear strain $\gamma + \delta\gamma$.
2. We switch off the soft potential, and equilibrate the system by using the LS algorithm to simulate the dynamics of HSs under the constant shear strain $\gamma + \delta\gamma$. The Lees-Edwards boundary condition is kept. We perform LS simulation for a duration δt , such that $\delta\gamma/\delta t = \dot{\gamma}$.
3. The above two steps are repeated until the shear strain reaches a target value.

To simulate quasi-static shear, we choose a sufficiently small $\dot{\gamma} = 10^{-4}$. We have checked that for $\varphi < \varphi_g$, the stress-strain response is independent of $\dot{\gamma}$ when $\dot{\gamma}$ is decreased from 10^{-3} to 10^{-5} (see Sect. D 1).

b. Instantaneous shear

To simulate instantaneous shear, we instantaneously increase the shear strain from 0 to γ . We then turn on the harmonic soft-potential, and use the CG algorithm to remove the overlaps. Different from the quasi-static shear, the system is generally far away from equilibrium after the instantaneous shear.

Appendix C: Quasi-static shear on equilibrium configurations

First let us report data obtained by quasi-static shear on *equilibrium* configurations at a few different φ_g (Fig. 6). As we noted in the main text, the system is in the liquid state in the thermodynamic sense (the Kauzmann density φ_K , if any, is larger than φ_g), but the α -relaxation time is much larger than our simulation time scales so that the system behaves as a solid. The stress-strain curve shows a linear elastic regime at small γ , followed by yielding. We define the location of the peak in the stress-strain curve as the yield strain γ_y . The shear modulus μ is determined by $\mu = \sigma/\gamma$ in the elastic regime. Both γ_y and μ grow with φ_g (Fig. 7). The yield strain γ_y and the yield stress σ_y , which is the stress at γ_y appear to vanish continuously around $\varphi_g \approx \varphi_d$. On the other hand, the shear modulus μ appears to remain finite at φ_d , which implies discontinuous jump of μ at φ_d being consistent with the mean-field theory [10]. In the elastic regime, the dilatancy effect is observed: the pressure p increases quadratically with γ , i.e., $p = p_g + R\gamma^2$, where p_g is the pressure at φ_g and $\gamma = 0$, and R is the dilatancy parameter. The onset of the peak in the pressure-strain curves lags behind the yielding. We compare our numerical data to the mean-field theoretical prediction [17], and find reasonable agreement on rescaled plots as shown in Fig. 6.

Appendix D: Quasi-static shear on out-of-equilibrium configurations

1. Stress-strain curves

Next, let us present quasi-static shear data of *out-of-equilibrium* configurations. These configurations are obtained by compressing equilibrium configurations from φ_g to a target density φ , at a constant compression rate $\delta_g = 10^{-3}$.

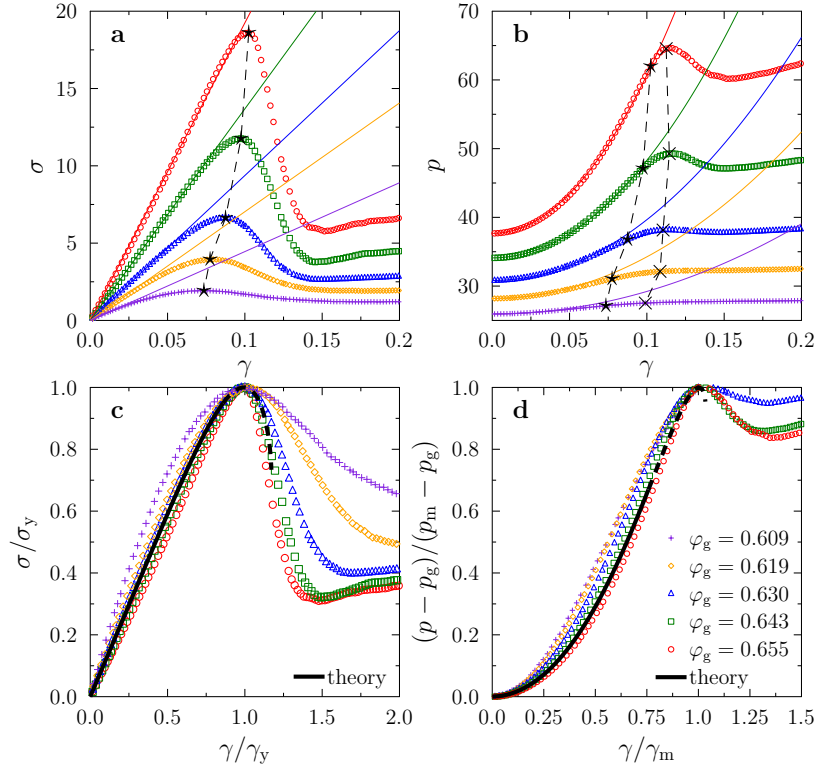


FIG. 6. Quasi-static shear on equilibrium configurations prepared at a few different φ_g . The systems consist of $N = 1000$ particles, and the data are averaged over $N_s = 100$ samples and $N_{th} = 10 - 20$ realizations for each sample. (a) The shear stress σ and (b) the pressure p are plotted as functions of the shear strain γ . At small γ , the stress-strain curve is fitted to a linear function $\sigma = \mu\gamma$ (lines), and the pressure-strain curve is fitted to a quadratic function $p = p_g + R\gamma^2$ (lines). The star marks the peak of the stress-strain curve, which represents the yielding point (γ_y, σ_y) , and the cross marks the peak (γ_m, p_m) of the pressure-strain curve. The parameters μ , γ_y , σ_y , γ_m , p_m , and R are reported in Fig. 7 as functions of φ_g . (c) The rescaled stress-strain curves and (d) the rescaled pressure-strain curves are compared to the mean-field theoretical predictions (black line) [17], for the equilibrium volume fraction $\hat{\varphi}_g = 2^d \varphi_g / d = 7$ in d -dimensions. Here the solid line part is shear replica symmetry breaking (1RSB) solution, and the dashed line part is the unstable 1RSB solution [17]. We have checked that the theoretical results are insensitive to $\hat{\varphi}_g$ on these rescaled plots.

Figure 8a shows that at small γ , the average stress-strain curve has a linear regime, which shrinks with increasing φ . Note that the data presented here are obtained by averaging over many samples and realizations, while the data in Fig. 1 (main text) are for one single sample and one single realization. For $\varphi > \varphi_G$, the apparent linear regime in Fig. 8a is not truly elastic, since it is averaged over many plastic micro-yielding events (Fig. 1). Thus the shear modulus defined as $\mu = \sigma/\gamma$ in the linear regime is not only due to purely harmonic responses but also involves non-affine corrections due to the plastic events. With this point being clarified, we show that the shear modulus μ obtained from fitting the data in the linear regime, is consistent with μ_{ZFC} presented in the main text (Fig. 8b).

At larger γ , we find that with increasing φ , the shear yielding disappears and the shear jamming emerges (Fig. 8a), which can be also observed in Fig. 1. Note that the simulation is performed under the constant volume condition. If we instead fix the pressure and allow the volume to change, then the shear jamming does not appear and the shear yielding exists, even at large φ (Fig. 9). We also stress that the shift from the shear yielding to the shear jamming is not correlated to the Gardner transition. In fact, Fig. 9 shows that it is possible to observe both micro-yielding (at small γ) and yielding (at large γ) in the same stress-strain curve. The key difference is that, after micro-yielding, the system remains in the same basin although it escapes from the sub-basin, and therefore it still behaves like a solid, while after yielding, the system escapes from the basin and essentially behaves like a fluid.

We next discuss in detail how the measurements of stress-strain curves depend on factors such as the compression rate δ_g , the shear rate $\dot{\gamma}$ (Fig. 10), the realization (Fig. 11), and the sample (Fig. 12). First of all, although these configurations are in principle out-of-equilibrium, they reach *quasi-restricted equilibrium* [17] for $\varphi < \varphi_G$, i.e., they are nearly equilibrated within their glass basins. As shown in Ref. [25], neither structural relaxation nor aging can be observed within the simulation time scale. According to that, in this regime, the results presented here should be nearly unchanged if a slower compression rate is used. The situation is different for $\varphi > \varphi_G$: because the time

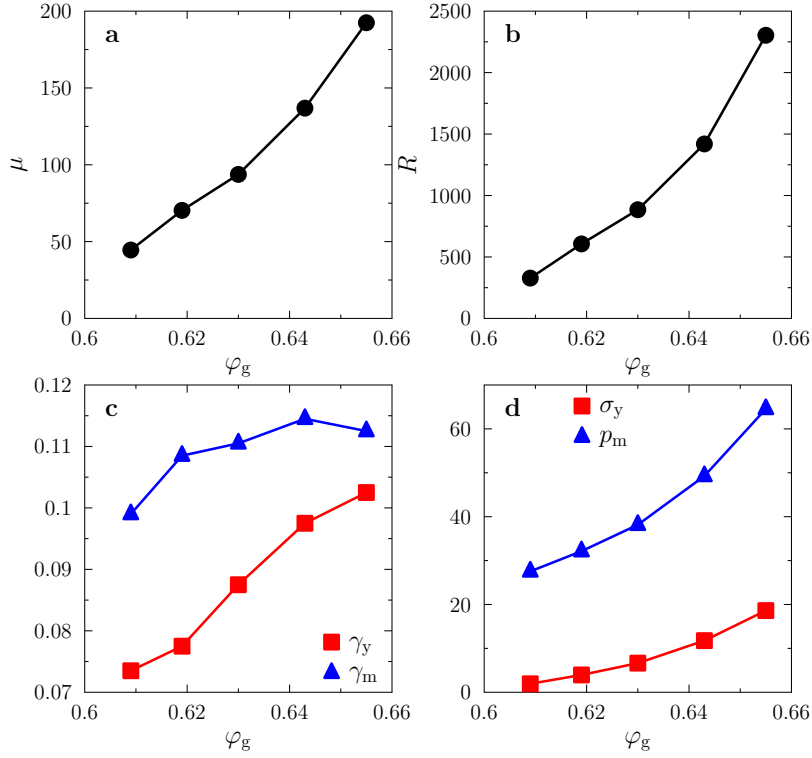


FIG. 7. Elastic and yielding parameters of equilibrium configurations. We plot as functions of φ_g , (a) the shear modulus μ , (b) the dilatancy parameter R , (c) the yield strain γ_y and the strain γ_m at the maximum pressure in the pressure-strain curve, and (d) the yield stress σ_y and the maximum pressure p_m .

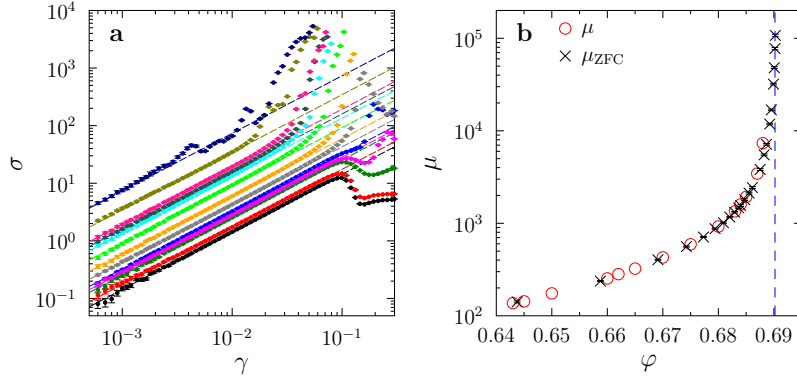


FIG. 8. Quasi-static shear on out-of-equilibrium glass states. The states are compressed from $\varphi_g = 0.643$ to target density φ before the shear is applied. The systems consist of $N = 1000$ particles, and the data are averaged over $N_s = 100$ samples and $N_{th} = 10 - 30$ realizations for each sample. (a) The shear stress σ as a function of γ , for a few different φ (from bottom to top, $\varphi = 0.645, 0.65, 0.66, 0.662, 0.665, 0.67, 0.675, 0.68, 0.683, 0.684, 0.685, 0.687, 0.688$). The linear response regime is fitted to $\sigma = \mu\gamma$ (lines). (b) The shear modulus μ obtained from this fitting is compared to the ZFC shear modulus μ_{ZFC} (we use $\gamma = 2 \times 10^{-3}$, see the main text), both of which diverge approaching to the jamming limit $\varphi_J = 0.690(1)$ (vertical dashed line).

scale diverges in this regime, it is difficult to obtain even the restricted equilibrium configurations and the data would be δ_g -dependent. Effectively, decreasing δ_g is equivalent to increasing the waiting time t_w . Since the δ_g -dependence has been well studied in previous work [25], we do not repeat the analysis here. For other factors, in the regime $\varphi < \varphi_G$, our results are independent of the shear rate (Fig. 10) and realizations (Fig. 11), although noticeable sample-to-sample variance (Fig. 12) is observed. In contrast, for $\varphi > \varphi_G$, the stress-strain curve is realization-dependent. This observation is consistent with our basic expectation: the free energy landscape is complex in this regime, and the system could fall into different sub-basins after compression.

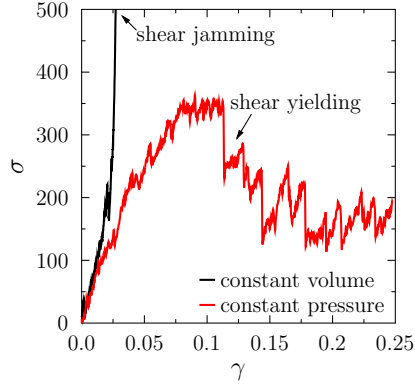


FIG. 9. Quasi-static shear on the same glass state ($\varphi_g = 0.643$, $\varphi = 0.688$, and $N = 1000$) under constant volume and constant pressure show different behaviors at large γ . We observe shear jamming in the constant volume simulation and shear yielding in the constant pressure simulation.

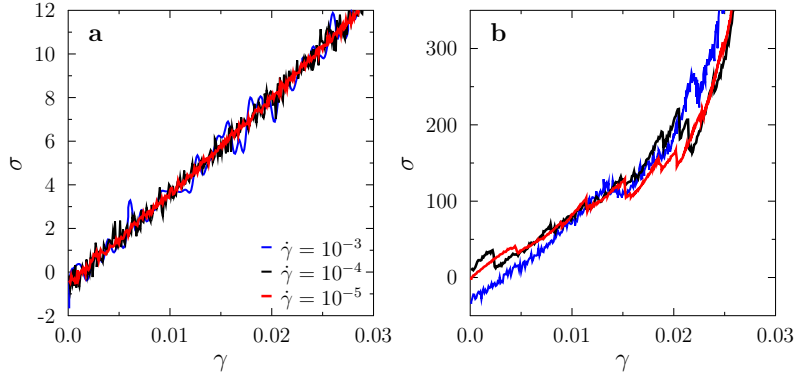


FIG. 10. The stress-strain curves of three *different realizations* of the compressed glass at (a) $\varphi = 0.670$, and (b) $\varphi = 0.688$, obtained from the *same equilibrated sample* of $N = 1000$ particles at $\varphi_g = 0.643$. They are driven by *different strain rates* $\dot{\gamma}$ as indicated by the legend.

2. Relaxation of the shear stress

Let us examine how the shear stress relaxes after a small shear strain γ is applied quasi-statically (Fig. 13). The data shall be distinguished with those in Fig. 2, where an instantaneous shear strain is applied. For $\varphi < \varphi_G$, we do not see aging effects within our numerical accuracy. The zero-field compression (ZFC) and the field compression (FC) shear stresses converge quickly to the same value. For $\varphi > \varphi_G$, no converge is observed within our simulation time window. The $\sigma_{\text{ZFC}}(\tau, t_w)$ displays a plateau for short τ , followed by slow decay. Note that the time scale $\tau = 1$ used in determining μ_{ZFC} (see main text) is in the plateau region.

Appendix E: Additional data on the protocol-dependent shear modulus

Here we report supplementary data on the protocol-dependent shear modulus. We discuss the φ_g -dependence on the ZFC and the FC shear moduli, and provide the shear modulus obtained from a third protocol.

1. φ_g -dependence

We find that our basic observation – the bifurcation between the ZFC shear modulus μ_{ZFC} and the FC shear modulus μ_{FC} at the Gardner transition φ_G – is independent of the initial equilibrium density φ_g (see Fig. 14). Note that the value of φ_G itself depends on φ_g . The large pressure ($\varphi \gg \varphi_G$) scalings, μ_{ZFC} versus p , and μ_{FC} versus p , are nearly unchanged for different φ_g . Additionally, we compare our simulation data with theoretical predictions

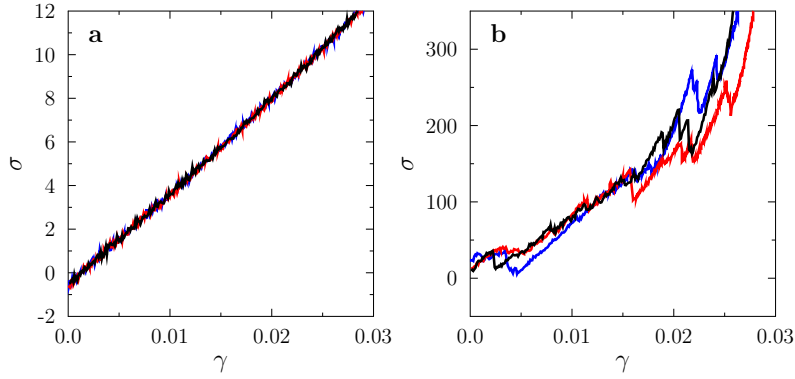


FIG. 11. Stress-strain curves of three *different realizations* of the compressed glass at (a) $\varphi = 0.670$, and (b) $\varphi = 0.688$, obtained from the *same equilibrated sample* of $N = 1000$ particles at $\varphi_g = 0.643$. They are driven by the *same strain rate* $\dot{\gamma} = 5 \times 10^{-6}$ for $\varphi = 0.670$, and $\dot{\gamma} = 10^{-4}$ for $\varphi = 0.688$.

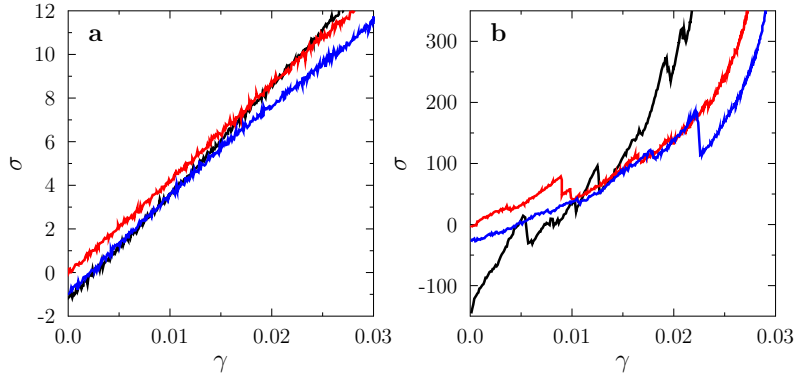


FIG. 12. Stress-strain curves on the compressed glasses at (a) $\varphi = 0.670$, and (b) $\varphi = 0.688$, obtained from three *different equilibrated samples* of $N = 1000$ particles at $\varphi_g = 0.643$. They are driven by the *same strain rate* $\dot{\gamma} = 5 \times 10^{-6}$ for $\varphi = 0.670$, and $\dot{\gamma} = 10^{-4}$ for $\varphi = 0.688$.

for $\varphi < \varphi_G$. We plot $\tilde{\mu}_{\text{ZFC}}/\tilde{\mu}_g$ and $\tilde{\mu}_{\text{FC}}/\tilde{\mu}_g$ as functions of p/p_g obtained from simulations, together with the mean-field *state following* theory [17], where $\tilde{\mu} = \mu/p$ is the modulus rescaled by the pressure, and μ_g and p_g are the shear modulus and the pressure at φ_g . Note that the theory does not distinguish between ZFC and FC moduli in this regime. On this rescaled plot, the theory and the simulation data show similar behaviors, both of which are insensitive to φ_g . We point out that the mean-field theory uses an over-simplified liquid EOS, that is only valid for mono-disperse hard spheres in the large dimensional limit. Thus a direct comparison between the theory and our simulation is impossible. However, once the effect of this mismatch on the liquid structure is removed by a proper rescaling with respect to the reference point at φ_g , the theory basically captures the general trend on how the system evolves under a slow compression annealing.

2. A third protocol

To further verify and emphasize the protocol dependence on the shear modulus, we design a third protocol, in which we apply an additional shear strain after the FC procedure. In this protocol, we first apply a small quasi-static strain γ at φ_g , compress the system to φ , and then after waiting for $t_w = 10$ and $\tau = 1$, we measure the stress σ_{FC} . This procedure is basically the same as the FC (see main text). We then apply an additional quasi-static strain γ at φ , and measure the stress σ_{FCS} after waiting for $\tau = 1$. The FCS (FC+shear) modulus is defined as $\mu_{\text{FCS}} = (\sigma_{\text{FCS}} - \sigma_{\text{FC}})/\gamma$. Figure 15 shows that this shear modulus is close to μ_{ZFC} , and clearly different from μ_{FC} . From the view point of free energy landscape, for $\varphi > \varphi_G$, μ_{FCS} represents the local curvature of the sub-basins at a finite given γ (see Fig. 4), while μ_{ZFC} is the local curvature of the sub-basins at $\gamma = 0$.

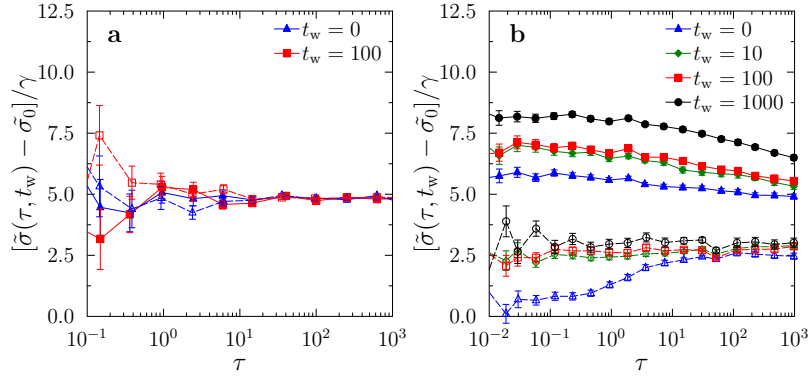


FIG. 13. Relaxation of $\tilde{\sigma}_{\text{ZFC}} = \sigma_{\text{ZFC}}/p$ (filled symbols) and $\tilde{\sigma}_{\text{FC}} = \sigma_{\text{FC}}/p$ (open symbols) at (a) $\varphi = 0.670$ and (b) $\varphi = 0.688$, for a few different t_w , under a quasi-static shear strain $\gamma = 10^{-3}$. The system consists of $N = 1000$ particles, and is compressed from $\varphi_g = 0.643$. The data are obtained for one individual sample, but averaged over $N_{\text{th}} \sim 1000$ independent realizations of the compressed glass. The remanent stress $\tilde{\sigma}_0$ has been subtracted from $\tilde{\sigma}$.

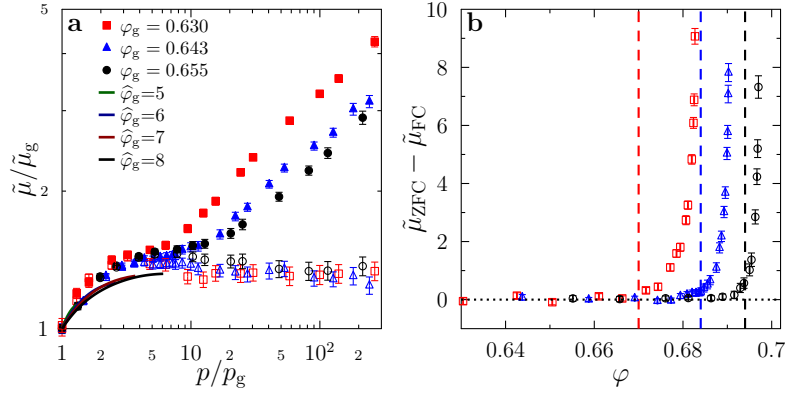


FIG. 14. φ_g -dependence on the ZFC and FC shear moduli. The data are obtained for $N = 1000$ particles, and are averaged over $N_s \approx 200$ samples and $N_r \approx 100$ individual realizations for each sample. To compute the shear modulus, $\gamma = 2 \times 10^{-3}$ is used. (a) The numerical data of the rescaled ZFC shear modulus $\tilde{\mu}_{\text{ZFC}} = \mu_{\text{ZFC}}/p$ (filled symbols) and the rescaled FC shear modulus $\tilde{\mu}_{\text{FC}} = \mu_{\text{FC}}/p$ (open symbols) with a few different φ_g , are compared to the mean-field theory (lines) with different $\hat{\varphi}_g$, where $\hat{\varphi}_g = 2^d \varphi_g/d$ in d dimensions, following the convention used in Ref. [17]. Both numerical and theoretical results are rescaled by the reference values $\tilde{\mu}_g = \mu_g/p_g$ and p_g at φ_g . (b) The difference $\tilde{\mu}_{\text{ZFC}} - \tilde{\mu}_{\text{FC}}$ as a function of φ for a few different φ_g , where the Gardner transitions φ_G (values from Ref. [25]) are marked by vertical lines.

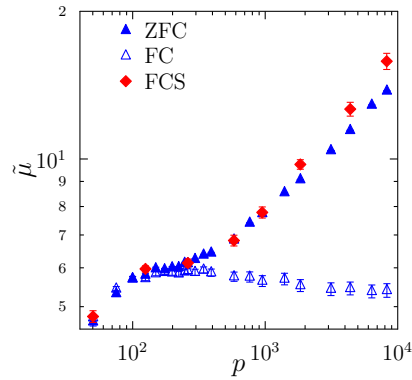


FIG. 15. The reduced shear modulus obtained from the third protocol (FCS) is compared to $\tilde{\mu}_{\text{ZFC}}$ and $\tilde{\mu}_{\text{FC}}$, for $\varphi_g = 0.643$, $N = 1000$, and $\gamma = 2 \times 10^{-3}$. The data are averaged over $N_s \approx 200$ samples and $N_r \approx 100$ individual realizations for each sample.

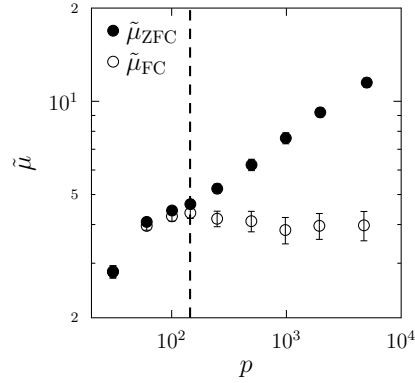


FIG. 16. Protocol-dependent shear modulus of a bidisperse hard disk glass former, where the vertical dashed line marks the Gardner transition estimated independently in Ref. [25]. The data are obtained for $\varphi_g = 0.808$, and are averaged over $N_s \approx 100$ samples and $N_{th} \approx 100$ realizations for each sample.

Appendix F: Protocol-dependent shear modulus of bidisperse hard disks

To test if the ZFC/FC approach can be applied to other systems, we also study a two-dimensional bidisperse hard disk model glass former. The system contains $N = 1000$ equimolar bidisperse hard disks with diameter ratio $D_1 : D_2 = 1.4 : 1$. The dynamical crossover density is $\varphi_d = 0.790(1)$ [25]. The example in Fig. 16 shows that the shear modulus becomes protocol-dependent for $\varphi > \varphi_G$. This signature can be used to determine φ_G , whose value is fully consistent with the previous independent estimate [25].

-
- [1] V K Malinovsky and A P Sokolov, “The nature of boson peak in Raman scattering in glasses,” *Solid State Commun.* **57**, 757–761 (1986).
 - [2] Dennis L. Malandro and Daniel J. Lacks, “Relationships of shear-induced changes in the potential energy landscape to the mechanical properties of ductile glasses,” *The Journal of Chemical Physics* **110**, 4593–4601 (1999).
 - [3] Gaël Combe and Jean-Noël Roux, “Strain versus stress in a model granular material: a devil’s staircase,” *Physical Review Letters* **85**, 3628 (2000).
 - [4] Ethan Pratt and Michael Dennin, “Nonlinear stress and fluctuation dynamics of sheared disordered wet foam,” *Physical Review E* **67**, 051402 (2003).
 - [5] CA Schuh and TG Nieh, “A nanoindentation study of serrated flow in bulk metallic glasses,” *Acta Materialia* **51**, 87–99 (2003).
 - [6] Craig E Maloney and Anaël Lemaître, “Amorphous systems in athermal, quasistatic shear,” *Physical Review E* **74**, 016118 (2006).
 - [7] H. G. E. Hentschel, S. Karmakar, E. Lerner, and I. Procaccia, “Do athermal amorphous solids exist?” *Phys. Rev. E* **83**, 061101 (2011).
 - [8] David Rodney, Anne Tanguy, and Damien Vandembroucq, “Modeling the mechanics of amorphous solids at different length scale and time scale,” *Modelling and Simulation in Materials Science and Engineering* **19**, 083001 (2011).
 - [9] Hajime Yoshino, “Replica theory of the rigidity of structural glasses,” *J. Chem. Phys* **136**, 214108 (2012).
 - [10] Hajime Yoshino and Francesco Zamponi, “Shear modulus of glasses: Results from the full replica-symmetry-breaking solution,” *Physical Review E* **90**, 022302 (2014).
 - [11] Michio Otsuki and Hisao Hayakawa, “Avalanche contribution to shear modulus of granular materials,” *Physical Review E* **90**, 042202 (2014).
 - [12] Markus Müller and Matthieu Wyart, “Marginal stability in structural, spin, and electron glasses,” *Annual Review of Condensed Matter Physics* **6**, 177–200 (2015).
 - [13] DV Denisov, KA Lörincz, JT Uhl, KA Dahmen, and P Schall, “Universality of slip avalanches in flowing granular matter,” *Nature communications* **7** (2016).
 - [14] Giulio Biroli and Pierfrancesco Urbani, “Breakdown of elasticity in amorphous solids,” *Nature Physics* (2016).
 - [15] Daiju Nakayama, Hajime Yoshino, and Francesco Zamponi, “Protocol-dependent shear modulus of amorphous solids,” *J. Stat. Mech.*, 104001 (2016).
 - [16] P. Charbonneau, J. Kurchan, G. Parisi, Pierfrancesco Urbani, and Francesco Zamponi, “Fractal free energy landscapes in structural glasses,” *Nat. Comm.* **5**, 3725 (2014).
 - [17] Corrado Rainone, Pierfrancesco Urbani, Hajime Yoshino, and Francesco Zamponi, “Following the evolution of hard sphere glasses in infinite dimensions under external perturbations: Compression and shear strain,” *Physical review letters* **114**,

- 015701 (2015).
- [18] Awadhesh K Dubey, Itamar Procaccia, Carmel ABZ Shor, and Murari Singh, “Elasticity in amorphous solids: Nonlinear or piecewise linear?” *Physical review letters* **116**, 085502 (2016).
 - [19] James P Sethna, Karin A Dahmen, and Christopher R Myers, “Crackling noise,” *Nature* **410**, 242–250 (2001).
 - [20] TG Mason, J Bibette, and DA Weitz, “Elasticity of compressed emulsions,” *Physical review letters* **75**, 2051 (1995).
 - [21] TG Mason, Martin-D Lacasse, Gary S Grest, Dov Levine, J Bibette, and DA Weitz, “Osmotic pressure and viscoelastic shear moduli of concentrated emulsions,” *Physical Review E* **56**, 3150 (1997).
 - [22] Carolina Brito and Matthieu Wyart, “On the rigidity of a hard-sphere glass near random close packing,” *EPL (Europhysics Letters)* **76**, 149 (2006).
 - [23] Corey S. O’Hern, Leonardo E. Silbert, Andrea J. Liu, and Sidney R. Nagel, “Jamming at zero temperature and zero applied stress: The epitome of disorder,” *Phys. Rev. E* **68**, 011306 (2003).
 - [24] Ludovic Berthier, Daniele Coslovich, Andrea Ninarello, and Misaki Ozawa, “Equilibrium sampling of hard spheres up to the jamming density and beyond,” *Phys. Rev. Lett.* **116**, 238002 (2016).
 - [25] Ludovic Berthier, Patrick Charbonneau, Yuliang Jin, Giorgio Parisi, Beatriz Seoane, and Francesco Zamponi, “Growing timescales and lengthscales characterizing vibrations of amorphous solids,” *Proceedings of the National Academy of Sciences* **113**, 8397–8401 (2016).
 - [26] Monica Skoge, Aleksandar Donev, Frank H. Stillinger, and Salvatore Torquato, “Packing hyperspheres in high-dimensional Euclidean spaces,” *Phys. Rev. E* **74**, 041127 (2006).
 - [27] Tomás Pérez-Castañeda, Cristian Rodríguez-Tinoco, Javier Rodríguez-Viejo, and Miguel A Ramos, “Suppression of tunneling two-level systems in ultrastable glasses of indomethacin,” *Proc. Nat. Acad. Sci. U.S.A.* **111**, 11275–11280 (2014).
 - [28] X. Liu, D. R. Queen, T. H. Metcalf, J. E. Karel, and F. Hellman, “Hydrogen-free amorphous silicon with no tunneling states,” *Phys. Rev. Lett.* **113**, 025503 (2014).
 - [29] H. B. Yu, M. Tylinski, A. Guiseppi-Elie, M. D. Ediger, and R. Richert, “Suppression of β relaxation in vapor-deposited ultrastable glasses,” *Phys. Rev. Lett.* **115**, 185501 (2015).
 - [30] Shoichi Nagata, PH Keesom, and HR Harrison, “Low-dc-field susceptibility of cu mn spin glass,” *Physical Review B* **19**, 1633 (1979).
 - [31] Jean-Philippe Bouchaud, Leticia F Cugliandolo, Jorge Kurchan, and Marc Mezard, “Out of equilibrium dynamics in spin-glasses and other glassy systems,” *Spin glasses and random fields*, 161–223 (1998).
 - [32] Antoine Seguin and Olivier Dauchot, “Experimental evidences of the gardner phase in a granular glass,” *arXiv preprint arXiv:1605.00827* (2016).
 - [33] HB Yu, M Tylinski, A Guiseppi-Elie, MD Ediger, and Ranko Richert, “Suppression of β relaxation in vapor-deposited ultrastable glasses,” *Physical review letters* **115**, 185501 (2015).
 - [34] M Paluch, CM Roland, S Pawlus, J Ziolo, and KL Ngai, “Does the arrhenius temperature dependence of the johari-goldstein relaxation persist above T_g ?” *Physical review letters* **91**, 115701 (2003).
 - [35] Jing Zhao, Sindee L Simon, and Gregory B McKenna, “Using 20-million-year-old amber to test the super-arrhenius behaviour of glass-forming systems,” *Nature communications* **4**, 1783 (2013).
 - [36] T. Boublik, “Hard sphere equation of state,” *J. Chem. Phys.* **53**, 471 (1970).
 - [37] William H Press, *Numerical recipes 3rd edition: The art of scientific computing* (Cambridge university press, 2007).
 - [38] AW Lees and SF Edwards, “The computer study of transport processes under extreme conditions,” *Journal of Physics C: Solid State Physics* **5**, 1921 (1972).